ACS APPLIED MATERIALS & INTERFACES

www.acsami.org Research Article

Lithium Dendrite Propagation in Ta-Doped $Li_7La_3Zr_2O_{12}$ (LLZTO): Comparison of Reactively Sintered Pyrochlore-to-Garnet *vs* LLZTO by Solid-State Reaction and Conventional Sintering

Jinzhao Guo and Candace K. Chan*

Cite This: *ACS Appl. Mater. Interfaces* 2024, 16, 4519–4529 Read Online

ACCESS | Metrics & More | Article Recommendations | Supporting Information

ABSTRACT: Ta-doped $Li_7La_3Zr_2O_{12}$ (LLZTO) garnet is a promising Li-ion-conducting ceramic electrolyte for solid-state batteries. However, it is still challenging to use LLZTO in Li metal batteries operating at high current densities because of the tendency for Li metal to nucleate and propagate along the grain boundaries. In this study, we carry out a detailed investigation to elucidate the effect of microstructure and grain size on the electrochemical properties and short circuit behavior in LLZTO. Pellets were prepared using reactive sintering from pyrochlore precursors (a method called pyrochlore-to-garnet, P2G) and compared with LLZTO synthesized using solid-state reaction (SSR) followed by conventional pressureless sintering. Both preparation methods were controlled to keep the phase and elemental composition, ionic and electronic conductivity, relative density, and area-specific resistance of the pellets constant. Reflection electron energy loss spectroscopy and X-ray photoelectron spectroscopy confirm that both types of LLZTO have similar band gaps and chemical states. Microstructure analysis shows that the P2G method results in LLZTO with an average grain size of around 3 μm, which is much smaller than the grain sizes (as large as 20 μm) seen in SSR LLZTO. Galvanostatic Li stripping/plating and linear sweep voltammetry measurements show that P2G LLZTO can withstand higher critical current densities (up to 0.4 mA/cm^2 in bidirectional cycling and >1 mA/cm^2 for unidirectional) than those seen in SSR LLZTO. Post-mortem examination reveals much less Li deposition along the grain boundaries of P2G LLZTO, particularly in the bulk of the pellet, compared to SSR LLZTO after cycling. The improved cycling behavior in P2G LLZTO despite the higher grain boundary area could be from more homogeneous current density at the interfaces and different grain boundary properties arising from the liquid-phase, reactive sintering method. These results suggest that the effect of grain size on Li dendrite propagation in LLZO may be highly dependent on the synthesis and sintering method employed.

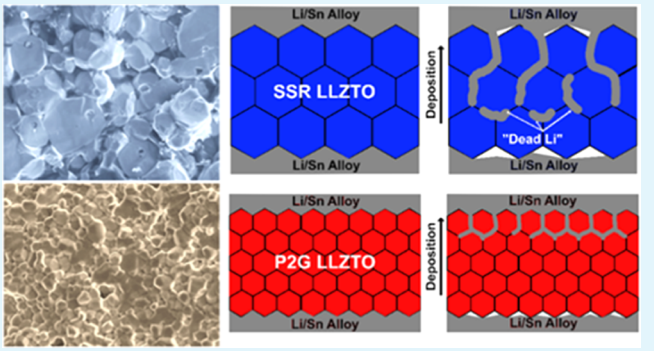

KEYWORDS: *lithium-ion battery, garnet, solid-state battery, liquid phase sintering, pyrochlore, grain boundary*

1. INTRODUCTION

Due to its high ionic conductivity (>10^{-4} S/cm)[1] at room temperature and chemical stability with lithium metal, garnet-type $Li_7La_3Zr_2O_{12}$ (LLZO) is considered a promising solid-state electrolyte material for lithium metal batteries. Among the various kinds of doped LLZO, Ta^{5+}-doped LLZO (LLZTO) is known to have good ionic conductivity and electrochemical stability.[2] LLZTO is commonly synthesized *via* solid-state reactions (SSRs) that require synthesis and then sintering at high temperatures (>1100 °C) for long durations (>6 h), which can be accompanied by Li loss and formation of poorly conducting phases.[3,4] To reduce the temperature and time required for both synthesis and sintering of LLZTO, we recently developed a new reactive sintering method that forms and densifies LLZTO from pyrochlore-type precursors in one step.[5,6] In this approach, which we call pyrochlore-to-garnet (P2G), Ta^{5+}-doped pyrochlore $La_{2.4}Zr_{1.12}Ta_{0.48}O_{7.04}$ is first synthesized using molten salt[5] or nonaqueous sol–gel methods[6] and then reacted with a Li source (typically LiOH) to obtain LLZTO. During the reactive sintering process, the LiOH melts and then decomposes into Li_2O,[7] which subsequently reacts with the pyrochlore to form LLZTO.

While the advantageous effects of smaller grain sizes on ionic conductivity have been demonstrated in other systems (*e.g.*, O^{2-} conducting CeO_2 electrolytes[8] and NASICON-type Li^+

Received: August 2, 2023
Revised: January 1, 2024
Accepted: January 2, 2024
Published: January 17, 2024

conductors),[9] the relationship between the grain size and the properties of LLZO is still unclear. Some early studies showed that LLZO pellets with smaller grain sizes can display higher ionic conductivity,[10] faster densification rates,[11] and improved cycling performance[12,13] and fracture strength.[14] For example, Cheng *et al.*[11,12] demonstrated a grain size effect on the LLZO air reactivity (*i.e.*, formation of surface Li_2CO_3 upon exposure to H_2O and CO_2), interfacial impedance, and critical current density (CCD), the current density above which Li metal filaments propagate and cause a short circuit. In those studies, a finer-grained LLZO microstructure (20−40 μm) was correlated with better properties (*e.g.*, lower interfacial resistance, reduced Li_2CO_3 formation, and higher CCD) compared to those of the large-grained (100−200 μm) LLZO. The improved CCD was explained by the more distributed Li^+ ion current density through LLZO pellets containing a larger number of grain boundaries (*i.e.*, from smaller grain sizes) compared to the more focused current at fewer failure points in LLZO with larger grain sizes. More recently, small-grained LLZO was later proposed to display grain boundaries with stronger bonding than large-grained LLZO[15] and less likely to exhibit interconnected or porous grain boundaries through which Li dendrites can grow.[16]

On the other hand, Sharafi *et al.*[17] investigated LLZO pellets prepared by hot-pressing and found that higher CCD could be sustained when the LLZO grain size increased from 5 to 600 μm. Studies on Li stripping/plating through LLZO have also shown that Li dendrites preferentially form along LLZO grain boundaries.[18−20] Recently, some grain boundaries in LLZO have been shown with smaller band gaps than the bulk[21−25] or defect states,[26] both of which could create local regions with high electronic conductivity that facilitate dendrite growth and short-circuits at grain boundaries. Theoretical[23,27] and experimental studies[28] have also shown that grain boundaries may trap electrons and nucleate the reduction of Li metal. Other studies showed that LLZO grain boundaries have much lower shear modulus than the bulk,[29,30] which can enable the penetration of Li metal dendrites. The grain boundaries can also display symmetry-dependent Li^+ conducting behavior.[31]

For all of these reasons, further investigation of the grain-size (and hence, grain boundary area) dependent properties of LLZTO is important for the development of better garnet-based electrolytes for Li metal batteries. In this work, the microstructure, relative density, and ionic conductivity of LLZTO prepared using the P2G method (from now on referred to as "P2G LLZTO") are evaluated and compared to those of LLZTO prepared using the conventional SSR method ("SSR LLZTO"). The synthetic conditions are controlled so that the two types of LLZTO have similar properties (*e.g.*, ionic and electronic conductivity, relative density, *etc.*) except for the grain size. The electrochemical characteristics of LLZTO pellets during Li stripping and plating are also compared to elucidate the influence of the different synthesis methods on the CCD. We find that P2G LLZTO, which has a smaller average grain size than SSR LLZTO, shows a longer cycling life and higher CCD during galvanostatic Li stripping and plating while also sustaining higher voltages in linear sweep voltammetry (LSV) measurements before shorting. Spectroscopic analysis using reflection electron energy loss spectroscopy (REELS) and X-ray photoelectron spectroscopy (XPS) does not provide evidence of differences in band gap or chemical state between the two types of LLZTO. We find that the smaller grain sizes and higher grain boundary area in P2G LLZTO do not lead to deleterious effects in terms of Li dendrite propagation and short circuit development when compared to SSR LLZTO. We propose that the smaller grain size in P2G LLZTO is beneficial for mitigating Li dendrite growth by homogenizing the Li flux, since there are more grain boundary pathways compared to that in larger-grained SSR LLZTO. The liquid-phase, reactive sintering process used in the P2G method may also lead to grain boundaries with different properties than those seen in LLZTO prepared using conventional sintering or hot-pressing.

2. EXPERIMENTAL SECTION

2.1. Preparation of LLZTO. P2G LLZTO was prepared from Ta-doped pyrochlores synthesized using a nonaqueous sol−gel method as described in our previous work.[6] Briefly, the pyrochlore was synthesized from a mixture of metal organic precursors dissolved in propionic acid and dichloromethane that was combusted at 850 °C for 8 h, followed by ball-milling with LiOH (25 mol % excess Li) and then pressing into a green pellet with uniaxial pressure at ∼300 MPa with a SpecAc press. SSR LLZTO was synthesized from Li_2CO_3 (Sigma-Aldrich, 99%), La_2O_3 (Aldrich, 99.99%), ZrO_2 (Aldrich, 99%), and Ta_2O_5 (Alfa Aesar, 99%). The raw materials were ball milled (SPEX 8000M, 1050 cycles per minute for 90 min) for good mixing, calcined at 950 °C for 12 h, ball milled again, and then prepared into a green pellet using uniaxial pressing at ∼300 MPa with a SpecAc press. The pellets were sintered in MgO crucibles under a Li_2O-rich environment, as described in our previous works,[6,32] in air using a tube furnace (Lindberg/Blue M TF55030A) with Al_2O_3 tubes and a heating rate of 5 °C/min. The P2G and SSR pellets were sintered at 1100 °C for 2 or 6 h, while some SSR pellets were also sintered at 1200 °C for 9 h. The nominal composition of both types of LLZTO was $Li_{6.4}La_3Zr_{1.4}Ta_{0.6}O_{12}$. The relative density of the pellet was determined from the weight, thickness, and cross-sectional area of the pellet and referenced to a theoretical density of 5.4 g/cm^3 (from the LLZTO reference pattern PDF 04-018-9024).[33] The pellets had diameters of around 6.5 mm and thicknesses of around 0.7 mm after sintering.

2.2. Materials Characterization. Powder X-ray diffraction (XRD) was performed on sintered LLZTO pellets (Malvern PANalytical Aeris) with a Cu Kα source after polishing with 240−2000 grit SiC sandpaper (McMaster-Carr) to obtain flat surfaces. The microstructure of the LLZTO samples was characterized using scanning electron microscopy (SEM) with a FEI XL30, FEI Nova 200, Zeiss Auriga, or Helios 5UX microscope. The elemental distribution was measured with an Oxford X-Max energy dispersive X-ray spectrometer using the Zeiss Auriga scanning electron microscope. The cross sections of the as-sintered samples were imaged by fracturing the pellets and coating the fracture surface with carbon using sputtering. To characterize samples after Li stripping/plating measurements, the pellets were first soaked in a solution of 3 M glacial acetic acid in isopropyl alcohol, followed by soaking in 1 M HCl to remove the Li/Sn alloy electrodes from the pellet surfaces. Then, the pellet fracture surfaces were imaged as described previously. The secondary electron image was used to observe the microstructure/morphology and the backscattered electron (BSE) image was used to indirectly identify Li dendrites. The average grain sizes of the LLZTO pellets prepared using P2G and SSR methods were measured from approximately 150 grains from SEM images (2000× magnification) of the fracture surfaces using ImageJ.

XPS was used to characterize the elemental composition and surface chemistry of the LLZTO samples by using a Kratos Axis Supra + spectrometer with a monochromatic Al Kα X-ray source. The pellet surfaces were polished with SiC sandpaper (similar process as described for XRD sample preparation) and further cleaned with 20 keV 500 Ar^+ clusters (equivalent to 40 eV Ar^+ ion, which should not reduce the elements in sample[34,35]). The binding energies were calibrated to the Zr 3d energy at 182.6 eV[36,37] because the C 1s signal was too weak after sample cleaning. The band gaps of sintered

https://doi.org/10.1021/acsami.3c11421
ACS Appl. Mater. Interfaces 2024, 16, 4519−4529

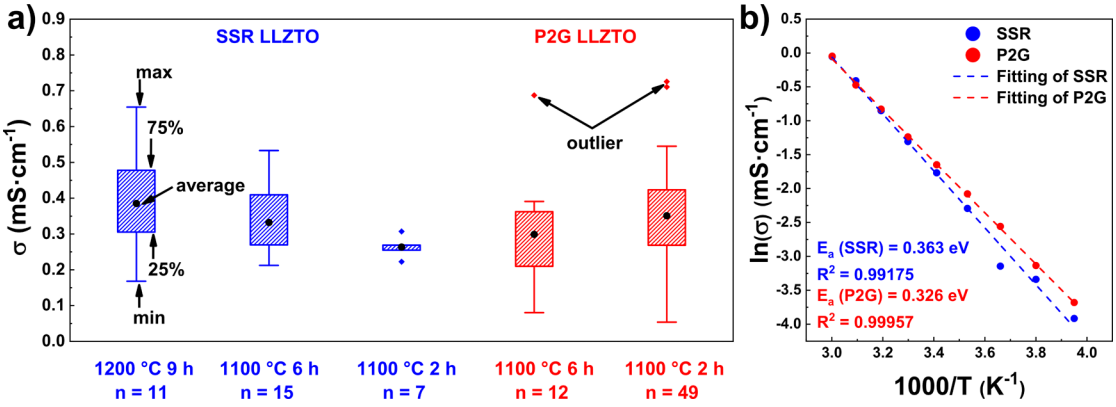

Figure 1. (a) Total ionic conductivities of LLZTO pellets (n = number of pellets) with different sintering conditions. (b) Arrhenius plot of the total ionic conductivity of P2G and SSR LLZTO. The dashed lines show fits according to the Arrhenius equation.

LLZTO samples were measured by XPS using REELS[38,39] from the low-energy (<50 eV) electron loss spectrum. Both XPS spectra and REELS analysis were taken from 200 μm × 200 μm areas on the surface of the pellet samples.

2.3. Electrochemical Characterization. The as-sintered pellets were polished under ambient conditions using a series of SiC sandpapers from 240 to 2000 grit (McMaster-Carr) to make clean and smooth surfaces. Then, the pellets were transferred to an Ar-filled glovebox for the application of Li/Sn alloy (20 wt % or ∼1.5 mol % Sn) on both sides (∼100 μm thick) of the pellet to serve as low impedance electrical contacts, as described in previous studies.[32,40] Coated LLZTO pellets were assembled in pouch cells and then removed from the glovebox for further electrochemical tests. The details of the cell assembly are described in our previous works.[6,41] The ionic conductivity of the LLZTO pellets was determined using electrochemical impedance spectroscopy (EIS) over a frequency range of 7 MHz−1 Hz with a 50 mV stimulus voltage at room temperature. The impedance data were fit as described in our previous work.[41] The total conductivity values were measured from −20 to 60 °C inside a home-built chamber using thermoelectric (Peltier) modules to change the temperature. The activation energy (E_a) was calculated from the linear fit of the equation: $\sigma_{total}T = A' \exp(-E_a/k_BT)$, where σ_{total} is the total ionic conductivity, A' is the pre-exponential factor, k_B is Boltzmann's constant, and T is the absolute temperature.

Galvanostatic Li stripping−plating measurements were performed in symmetric configurations with Li/Sn alloy electrodes. Initially, the Li^+ was stripped (oxidized) from the counter electrode and moved to the working electrode to become reduced (Li metal plating). The direction of the current was reversed after 30 min or 1 h so that a full stripping/plating cycle was either 1 or 2 h. The voltage limit was set to −1.5 and +1.5 V. The pellets were cycled with an initial current density of ±0.05 mA/cm^2, which was increased to ±0.1, ±0.2, ±0.3, and ±0.4 mA/cm^2 until completing 50 cycles or short-circuiting. The amount of Li dissolved/plated in a unit area was calculated from Faraday's law using $n = \frac{It}{zF}$, where n is the number of moles of Li metal dissolved in a unit area, I is the current passed through the unit area, t is the time, z is the valence of the Li^+ ion, and F is Faraday's constant. The thickness of Li was calculated from the equation $T = \frac{nM}{\rho A}$, where T is the thickness of Li metal dissolved in a unit area, M is the atomic mass of Li, ρ is the density of Li, and A is the area. All experiments were carried out at room temperature and without any externally applied pressure to the pellets.

Linear scanning voltammetry (LSV) was also used to measure the current response of the symmetric cells under a unidirectional linear increase in voltage with a scan rate of 5 mV/s. When the current density of the cell showed a sudden increase, the cell was considered short-circuited; the voltage at which the short was observed is referred to as the "critical voltage" in this work. The electronic conductivity of the samples was measured using DC polarization as described in Han *et al.*'s work,[21] except instead of Cu contacts, graphite electrodes were applied as described in previous work.[32]

3. RESULTS

3.1. Ionic Conductivity, Microstructure, and Electronic Properties of P2G and SSR LLZTO. To elucidate the effect of grain size on the properties of LLZTO, we aimed to keep all other parameters (*e.g.*, phase purity, ionic conductivity, relative density, *etc.*) constant between the P2G and SSR materials. Figure 1a shows the ionic conductivities of SSR (blue) and P2G (red) LLZTO pellets sintered under different conditions. Both types of LLZTO were sintered at 1100 °C for 2 and 6 h, and SSR LLZTO was also sintered at 1200 °C for 9 h. The box plots show the ionic conductivity data for all samples (n = number of pellets per sintering condition). In these plots, the whiskers indicate the maximum and minimum values observed, the box shows data from the highest quarter to lowest quarter of values, and the average values are indicated by the black circles. The results show that the SSR LLZTO requires comparatively longer sintering times than P2G LLZTO to reach a similar average ionic conductivity. For P2G LLZTO, 2 and 6 h sintering at 1100 °C results in similar average room temperature ionic conductivity. The ionic conductivity of both types of LLZTO increases slightly with the relative density, and the relative density also slightly increases with the sintering time (Figure S1). EIS data for P2G and SSR pellets evaluated from −20 to 60 °C are presented in Figure S2. Based on the linear fit (Figure 1b) of ln (σ) and 1000/T, we found the activation energies to be 0.326 eV for P2G and 0.363 eV for SSR, which correspond well to the literature values.[32] At −20 °C, the Nyquist plots show a small feature attributed to the grain boundary resistance in the frequency range of 100−2 kHz, and the total ionic conductivities for P2G and SSR samples were also comparable (Figure S2d). Taking all data points into consideration, we can conclude that SSR LLZTO sintered at 1100 °C for 6 h has similar ionic conductivity to that of P2G LLZTO sintered at 1100 °C for 2 h. Hence, these two types of LLZTO pellets were chosen for further comparison and characterization.

The XRD patterns for a SSR LLZTO pellet sintered at 1100 °C for 6 h and a P2G LLZTO pellet sintered at 1100 °C for 2 h were similar (Figure S3) and matched well with the $Li_{6.5}La_3Zr_{1.5}Ta_{0.5}O_{12}$ reference pattern, indicating that both sintered pellets have high phase purity. Figure 2a shows that the average grain size was 2.9 μm (SD 1.02) for P2G LLZTO,

https://doi.org/10.1021/acsami.3c11421
ACS Appl. Mater. Interfaces 2024, 16, 4519−4529

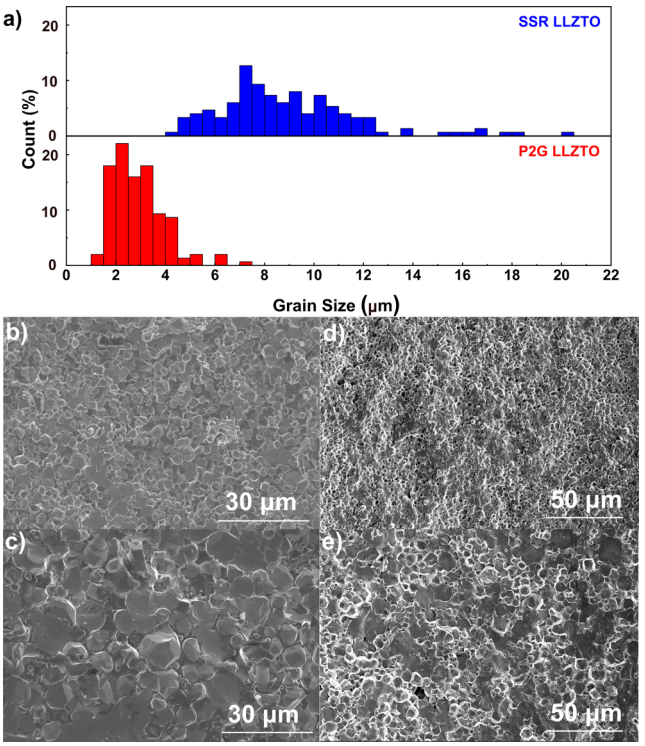

Figure 2. (a) Grain size distribution of SSR and P2G LLZTO pellets. SEM images at 2000x of (b) P2G LLZTO sintered at 1100 °C for 2 h and (c) SSR LLZTO sintered at 1100 °C for 6 h and at 1000x of the same pellets: (d) P2G and (e) SSR.

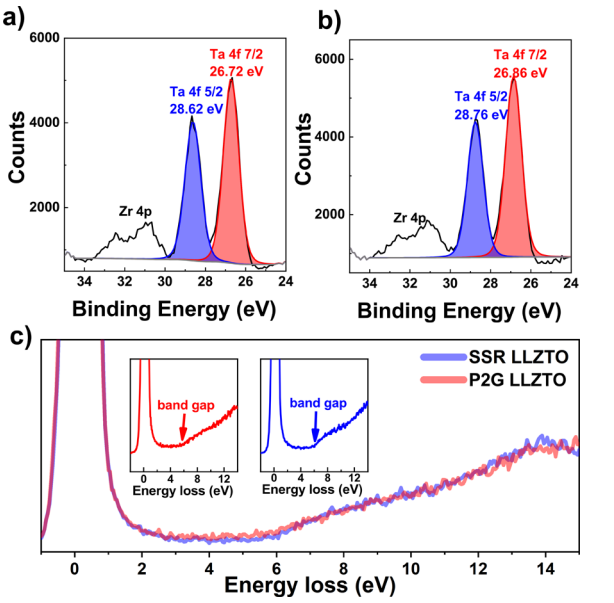

Figure 3. High-resolution XPS spectra of Zr 4p and Ta 4f for (a) SSR and (b) P2G LLZTO. (c) Valence REELS spectra of SSR LLZTO (blue) and P2G LLZTO (red) taken from a 200 μm × 200 μm area. Inset shows the position of the band gap region.

while it was 8.9 μm (SD 2.8) for SSR LLZTO, which also had a wider grain size distribution. As discussed in our previous works,[5,6] the smaller grain size in P2G LLZTO is attributed to the mechanism of garnet formation in the P2G method. During the reactive sintering process, LLZTO forms directly from the reaction of pyrochlore nanoparticles with molten LiOH in only 2 h, which allows for garnet formation and densification without substantial grain growth. The SEM images of the fracture surfaces of P2G LLZTO (Figure 2b,d) sintered at 1100 °C for 2 h and SSR LLZTO (Figure 2c,e) sintered at 1100 °C for 6 h show that both types of pellets are relatively dense with few inner pores.

To obtain more information about the electronic structure and chemical bonding in the LLZTO samples, XPS was performed. Due to the formation of Li_2CO_3 surface species when LLZTO is exposed to water and carbon dioxide under ambient conditions,[42] the carbon signal is very high for as-prepared pellets (even after polishing with sandpaper) and can block the observation of signals from the underlying LLZTO. The surfaces of the samples were cleaned using Ar^+ clusters to remove the Li_2CO_3 on the surface before the XPS analysis. After the Ar^+ cluster etching, the C−C signal was reduced to a very low level, indicating a significant removal of Li_2CO_3 (Figure S4). The Zr 3d peaks were therefore used for energy calibration instead of the C 1s peak and validated with a ZrO_2 reference (Figure S5). The XPS spectra of the Ta 4f peaks are shown in Figure 3a,b, with the feature at higher energy (~30.5 eV) representing the binding energy of Zr 4p.[43,44] The Ta 4f spectra in the P2G and SSR samples show very similar binding energy, areal ratio (4:3) between the Ta $4f^{7/2}$ and $4f^{5/2}$ peaks, and peak splitting (ΔE ~ 1.9 eV), which match the characteristics expected for Ta^{5+}.[44−49] Similarly, the La and Zr spectra for the P2G and SSR pellets were almost identical (Figure S6), showing that the oxidation states and chemical environments in the two types of samples are very similar.

Analysis of LLZTO using EELS has been informative for identifying local changes in the composition and band gaps at the grain boundaries.[25] Reflection electron energy loss (REELS) is a complementary technique that bombards low-energy photons onto the surface of sample and then collects the reflected electrons to measure their energy distribution.[50] In this work, REELS data were collected from 200 μm × 200 μm areas in the P2G and LLZTO pellets, and so the measurement is sampling many grains and grain boundaries. Figure 3c shows the valence REELS spectrum of SSR (blue) and P2G (red) LLZTO. The REELs spectra for both types of LLZTO are very similar, and both increase in intensity at ~6 eV, which corresponds to the band gap value.[38,51] This value is consistent with values from theoretical calculations (6.4 eV)[52] and optical absorption measurements (5.5 eV,[52] ~ 6 eV[51]). Electronic conductivity measurements (Figure S7) showed that the overall electronic conductivity of SSR and P2G LLZTO pellets are on the same level (SSR: 4.4 × 10^{-9} S/cm; P2G: 3.9 × 10^{-9} S/cm), which is within the range (10^{-7}−10^{-9} S/cm) of data reported by other groups for polycrystalline LLZO.[3,21,53,54]

3.2. Electrochemical Cycling Behavior of P2G *vs* SSR LLZTO. Galvanostatic Li stripping/plating measurements were carried out on P2G and SSR pellets by using Li/Sn alloy electrodes in symmetric cell configurations. The pellets had comparable relative densities and ionic conductivities (Table S1, Nyquist plots in Figure S8), with an average of 91.25% (SD 2.05) and 0.425 mS/cm (SD 0.16), respectively. This is similar to the range shown in Figure 1, so we consider these representative pellets. Figure 4 shows the voltage profiles for measurements carried out on P2G and SSR pellets with 1 h per full cycle (*e.g.*, 30 min stripping, 30 min plating) (Figure 4a,b) and 2 h per full cycle (Figure 4c,d) with zoomed in versions shown in Figures S9−S12. The cycling data show that the

https://doi.org/10.1021/acsami.3c11421
ACS Appl. Mater. Interfaces 2024, 16, 4519−4529

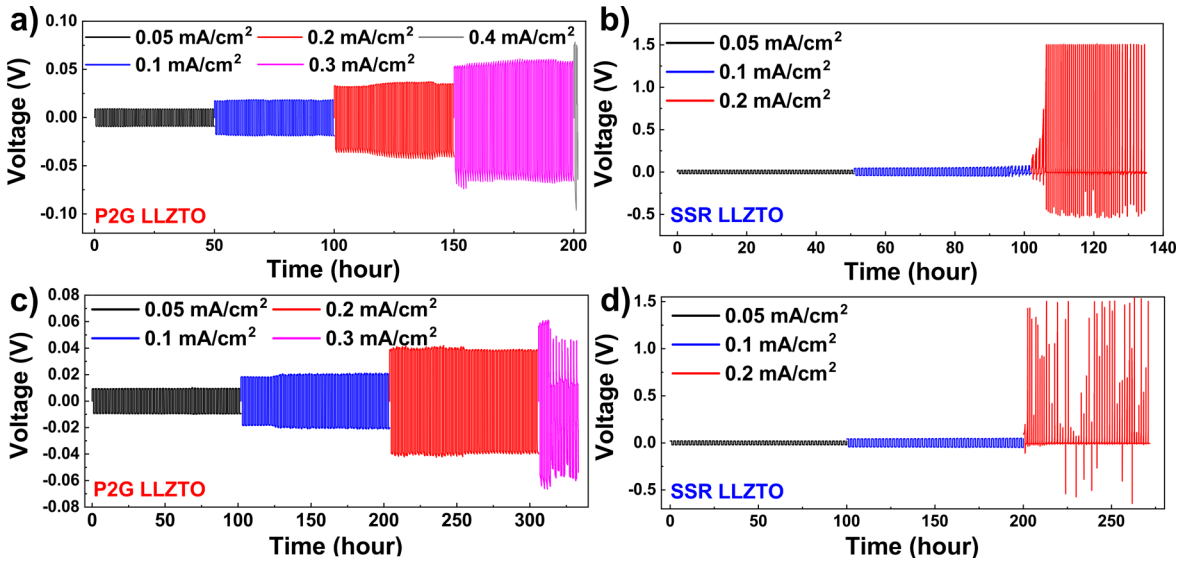

Figure 4. Voltage profiles of (a) P2G and (b) SSR LLZTO pellets under constant current cycling, 1 h per full cycle. Voltage profiles of (c) P2G and (d) LLZTO pellet under constant current cycling, 2 h per full cycle. The SSR LLZTO was sintered at 1100 °C for 6 h, while the P2G LLZTO was sintered at 1100 °C for 2 h.

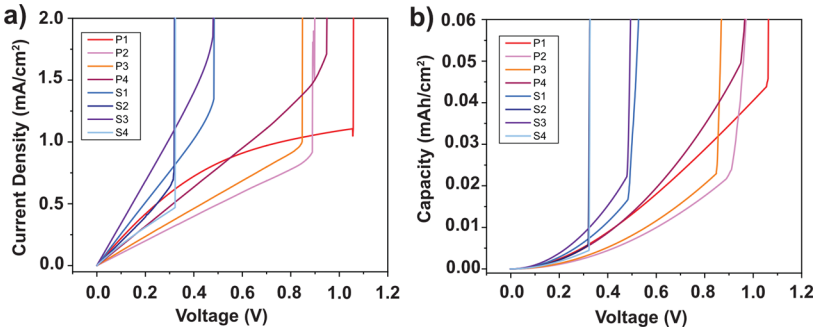

Figure 5. (a) Current density and (b) capacity profile of P2G and SSR LLZTO pellets during the LSV test. S1−S4 represents SSR pellets; P1−P4 represents P2G pellets.

maximum voltage values increase as the current density increases, but that the voltage response and CCD to cause shorting were different in the two types of LLZTO. We can see that in Figure 4a, the cycling was stable and the voltage of P2G LLZTO was relatively constant and showing ohmic behavior (see Figure S9 for zoomed-in views) at each current density up to 0.3 mA/cm^2, which indicates that there is no significant increase of internal resistance. However, a sudden voltage drop was observed (Figure S9e) when the current density was increased to 0.4 mA/cm^2, indicating short circuiting of the cell. For SSR LLZTO, the voltage profiles were stable at 0.05 mA/cm^2 but became sloped at 0.1 mA/cm^2 (Figure S10b), indicating an increase in resistance, with cells shorting at the end of cycling at 0.1 mA/cm^2 (Figures 4b and S10b). When the time of the full cycle was doubled (from 1 to 2 h), the P2G pellet showed a short circuit when the current density was increased to 0.3 mA/cm^2 (Figure 4c). The amount of Li dissolved/plated per unit area at 0.3 mA/cm^2 was calculated as 1.45 μm thick. However, the SSR pellet (Figure 4d) still short-circuited at 0.1 mA/cm^2. These experiments were repeated with other pellets (Figure S13 and Table S2), with the SSR LLZTO consistently shorting at lower current densities than P2G LLZTO.

As an alternative to galvanostatic cycling, LSV was also performed on P2G and SSR LLZTO pellets. LSV allows for polarization of the cell in one direction with a steady increase in current density until the formation of a short circuit, as indicated by a sharp increase in current density. As in the galvanostatic measurements, efforts were made to keep the physical properties of the pellets as close as possible so that the effect of the grain size could be isolated. Figure 5a,b shows the LSV current density and capacity profiles acquired using a scan rate of 5 mV/s, where P1−P4 are P2G pellets and S1−S4 are SSR pellets. The pellets had an average relative density around 88% and an ionic conductivity of around 0.3 mS/cm (Table S3), except for P1 (98% and 0.6 mS/cm). The results show that the P2G pellets generally display higher CCD values than the SSR pellets (Table S3), although there are pellet-to-pellet variations. During bidirectional cycling (as illustrated in Figure 4), the LLZTO/Li metal interface can worsen and cause the interface resistance to increase with repeated stripping/plating, eventually resulting in void formation and a decrease in the active interface area. However, since LSV is unidirectional, the interface where plating takes place should be void free. This is believed to be the reason for the higher CCDs seen in LSV measurements compared to the galvanostatic measurements.[55,56]

The SSR pellets also shorted at a "critical voltage" of ~0.3−0.5 V, similar to the findings by others,[55,56] where LSV on LLZTO prepared by SSR displayed shorting at ~0.4 V. In

https://doi.org/10.1021/acsami.3c11421
ACS Appl. Mater. Interfaces 2024, 16, 4519−4529

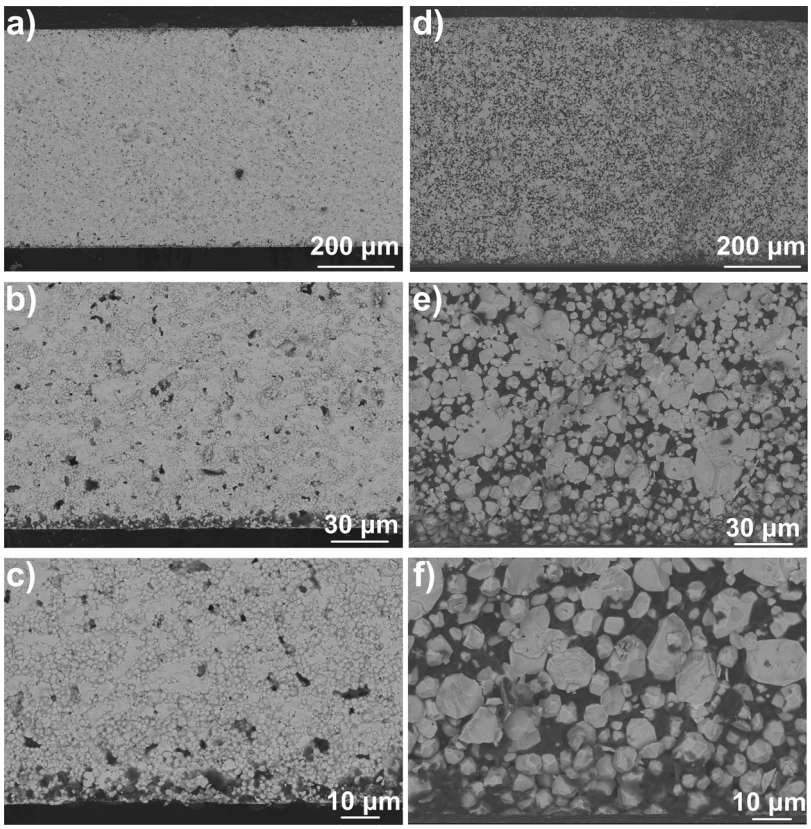

Figure 6. (a–c) Backscattered SEM image of the P2G LLZTO sample after cycling. (d–f) Backscattered SEM image of the SSR LLZTO sample after cycling. These pellets correspond to the pellets from Figure 4a (P2G) and 4b (SSR).

contrast, the critical voltage for the P2G pellets was more than doubled. P1, which had the highest relative density and ionic conductivity, showed a critical voltage of ~1 V and a CCD of 1.11 mA/cm^2. Based on the small amount of charge capacity passed during the LSV experiment (Figure 5b), a maximum of ~0.05 mA h/cm^2 for the best P2G pellets (equivalent to a ~ 240 nm thick Li layer) but as low as 0.005 mA h/cm^2 for the worst SSR pellet, we believe the interfaces should remain intact and free from voids. Finally, the differences in R_{tot} and R_i from the EIS data of the pellets taken prior to the LSV measurements (Figure S14 and Table S3) did not appear to have a large effect on the critical voltage. For instance, P2 had the highest R_i but a critical voltage larger than that of S1 and S2. As with the galvanostatic cycling measurement, the LSV results again show that P2G LLZTO displays better resistance to short-circuiting compared to SSR LLZTO despite the higher grain boundary area.

3.3. Microstructure Analysis of P2G and SSR LLZTO after Cycling. To better understand the distribution of Li metal through the pellets after short circuit formation, the pellets subjected to galvanostatic cycling were fractured, and cross-section samples were observed with SEM. Figure 6 shows the BSE cross-sectional images for LLZTO pellets (0.8–0.9 mm thickness) after the galvanostatic stripping/plating experiments. Figure 6a–c are SEM images of the P2G pellet from Figure 4a after cycling, while Figure 6d–f are the SEM images of the SSR pellet shown in Figure 4b after cycling.

In BSE imaging, the signal intensity increases with the increase in atomic number; therefore, the regions with dark contrast in these images are presumed to be from lithium-containing species, *e.g.* LiOH, Li_2O, or Li_2CO_3, that formed when the pellet was fractured and the deposited Li metal was exposed to the air. The low magnification BSE images show that there are fewer dark areas in P2G LLZTO (Figure 6a) than in SSR LLZTO after shorting (Figure 6d), especially near the center or bulk of the pellet far from the interface with the Li/Sn electrodes. Under higher magnification (Figure 6b,c), Li appears to be deposited very uniformly along the edge of the P2G pellet with the majority of LLZTO grains still in contact with each other. Also, while Li can be found in some pores and voids, there is no significant Li found along the grain boundaries in the bulk of the P2G LLZTO pellet.

In contrast, for SSR LLZTO, significant regions of dark contrast are seen throughout the pellet and in the bulk (Figure 6e,f), with most grains appearing to be completely surrounded by Li. These results seem to indicate that the contacts between SSR LLZTO grains are more easily penetrated by Li during cycling, which further augments the destruction of the structure. Based on the theoretical calculation for the amount of Li deposited during plating, there should only be, at most, a 1–2 μm thick Li layer deposited in each cycle, which is not enough to build a network of Li filaments, as seen in Figure 6d–f. A plausible explanation is that only a small portion of the Li deposited in SSR LLZTO was stripped back to the interface in each cycle, with the rest of the Li becoming disconnected from the electrodes (*i.e.*, becoming "dead Li") and staying in the pellet. With each subsequent cycle, more dead Li can form and finally build a large network of Li dendrites.

The failure mechanism *via* intragranular Li metal propagation observed in SSR LLZTO is reproduced in multiple pellets (Figures S15 and S16) and consistent with observations from other reports.[18,20] We observed that in some SSR pellets

https://doi.org/10.1021/acsami.3c11421
ACS Appl. Mater. Interfaces 2024, 16, 4519–4529

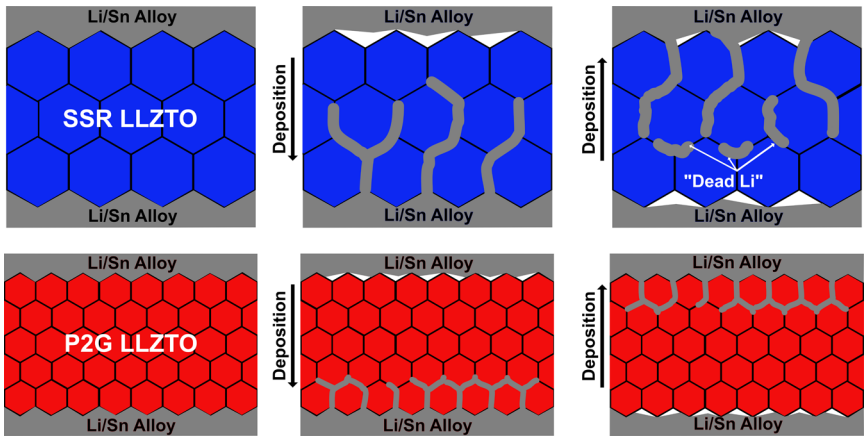

Figure 7. Schematic of proposed lithium stripping/plating processes in larger-grained SSR LLZTO compared to smaller-grained P2G LLZTO.

(*e.g.*, the pellet corresponding to the data in Figure S13d), energy-dispersive X-ray spectrometry (EDS) analysis revealed the presence of Mg and Al at the grain boundaries (Figure S17a,b). We suspect that this arose due to adventitious contamination from the MgO crucible and/or Al_2O_3 tube used for the sintering since these impurities were not seen in the as-synthesized SSR powder (Figure S17c). Segregation of Al-containing glassy phases at the grain boundaries of LLZTO from unintentional and intentional doping has been reported in previous studies.[57,58] Such contamination was not seen in either the pyrochlore precursor or the P2G pellets, likely because of the shorter required calcination/sintering times in the P2G method (Figure S18). SSR pellets without Mg/Al impurities displayed similar ionic conductivity and cycling properties (Figure S19) to the pellets with contamination, which suggests that these impurities do not play a major role in the short-circuit behavior in the SSR pellets prepared herein.

On the other hand, the absence of significant Li metal signatures around the grain boundaries in P2G LLZTO is in stark contrast to the failure mode seen in SSR LLZTO. We acknowledge that the SEM images only show a single fracture surface, and that there must be a dendrite causing a short circuit in some other plane of view. Figures S20−S22 shows SEM images at different magnifications of a P2G pellet where a Li metal dendrite was observed in a crack visible in the fracture plane. Despite the large crack-embedded Li dendrite, there is still a noticeable absence of Li around the grain boundaries. These microstructural observations, along with the higher CCDs achieved in the P2G pellets in the electrochemical tests, strongly suggest a lower concentration of Li dendrites in these samples. The results point to an improved resistance to failure by Li dendrite penetration in P2G LLZTO despite the small grain size and larger grain boundary area in these materials.

4. DISCUSSION

Given that Li dendrites are known to nucleate at and penetrate through the grain boundaries of LLZO, one may expect samples with smaller grains to display lower CCDs and worse resistance to short circuits. However, our experimental data show that P2G LLZTO can exhibit improved Li stripping/plating characteristics compared to SSR LLZTO, which suggests that any potential disadvantages of small grain size or large grain boundary area may be avoided in P2G LLZTO. Theoretical calculations[23,27] and EELS measurements[25] previously showed that the surfaces and grain boundaries in LLZTO exhibit lower band gaps than the grain volumes, but from the XPS measurements collected herein, we are unable to observe significant differences in chemical oxidation state or average band gaps from REELs. While we acknowledge that our XPS and REELS measurements may be limited in spatial resolution, the galvanostatic cycling, LSV measurements, and post-mortem SEM analysis are all consistent and point to an improved resistance to Li nucleation and propagation at grain boundaries in P2G samples, leading to higher sustained current density and voltage before short circuit formation when compared to SSR LLZTO. Therefore, there must be some other reason to explain the observed differences in the P2G and SSR pellets.

The role of electronic conductivity in the nucleation and propagation of Li dendrites through the LLZO has been the subject of much discussion. Theoretical calculations provide support for the ability of LLZO surfaces to trap excess electrons,[27] enabling the nucleation of isolated Li metal in pores or voids. However, the fact that Li dendrite formation is also observed in highly dense samples has drawn attention to the role of electronic conductivity in LLZO. Measurements conducted on chemically homogeneous single crystals of Ga-doped LLZO revealed a much lower electronic conductivity of $\sim 10^{-10}$ S/cm[59] compared to those measured on polycrystalline samples, while first-principles calculations predicted an even lower intrinsic electronic conductivity of $<10^{-18}$ S/cm.[60] Since the electronic conductivity of as-prepared P2G and SSR pellets in our study are comparable (Figure S7), we posit that, at least in the samples studied herein, the electronic conductivity of the grain boundaries is not the origin of the difference we observe in the electrochemical properties of the two samples.

Another important parameter is the area-specific resistance (ASR) of the interface. The Li/LLZO interface is known to display high resistance due to poor wetting of Li to the surface of LLZO, and the CCD and ASR are usually inversely correlated.[61] The CCDs observed herein also appear to be consistent with or higher than what has been reported by other groups for similar values of ASR.[62] While some P2G pellets display a lower ASR than the SSR pellets, there does not appear to be a strong correlation between the ASR and the CCD from our data.

We propose that the grain size reduction in P2G samples is beneficial for mitigating Li dendrite growth by homogenizing the Li flux and distributing the current, as shown schematically in Figure 7, where there are more grain boundary pathways for

https://doi.org/10.1021/acsami.3c11421
ACS Appl. Mater. Interfaces 2024, 16, 4519−4529

the Li dendrites to distribute over in fine-grained LLZTO compared to large-grained LLZTO. This is similar to the results and explanation reported by Cheng *et al.*, where fine-grained LLZTO was prepared by attrition milling of SSR powders and displayed improved cycling performance compared to large-grained samples.[13] Ouyang *et al.* arrived at a similar conclusion and further highlighted the benefit of using small-grained LLZO with minimal pores to achieve higher CCD compared to that achieved using large-grained LLZO.[56] Su *et al.* also showed that fine-grained Ga-doped LLZO prepared using two-step sintering displayed better resistance to cracking after exposure to Li compared to samples with larger grains, some of which displayed abnormal grain growth.[63] The authors proposed that LLZO pellets with more homogeneous grain size can endure higher stresses, since such cracks could form from lattice volume changes when Li enters the LLZO structure. Additionally, since it has been shown through density functional theory calculations that LLZO with different surface terminations have different adhesion energies and hence wettability to Li metal,[64] and smaller grain sizes could decrease the contact area between Li and the poorly wetting grains. Another difference might be that for smaller grain sizes, the Li dendrites grown during the cycling may be less likely to become disconnected and turn into "dead Li".

We also speculate that the fine-grained LLZTO afforded by our P2G method may lead to grain boundaries with properties different from those seen in conventional SSR LLZTO or even fine-grained pellets prepared using other methods such as two-step sintering. There are two possible reasons for this. The first is that P2G LLZTO is formed *via* the reactive sintering of the pyrochlore precursor with LiOH, which is molten at the sintering temperature used in our studies. Liquid-phase sintering is known to not only improve densification of powders using shorter sintering times but may also lead to different microstructures compared to conventional sintering.[65] In our P2G process, the amount of LiOH in the green pellet is estimated to be at least 50 vol % once melted; we speculate that the large volume of liquid phase can allow for the formation of LLZTO with lower energy surfaces. This can be seen in the fracture surfaces of the P2G pellets (Figure S23), which exhibit predominantly intergranular fracture to reveal faceted grains resembling the trapezohedral and dodecahedral crystal habits seen in naturally occurring garnet silicate minerals (Figure S24).[66] In contrast, the fracture surface of SSR LLZTO displays more transgranular (intragranular) fracture, particularly in the larger grains. While more research is needed to better understand the nature of the grain boundaries in the P2G samples, we hypothesize that they may also be different from those in LLZO prepared by rapid densification methods such as hot-pressing. Electron backscattered diffraction studies on hot-pressed LLZO have shown that grain boundaries with higher misorientation angles (>40 to 50°) are more favorable than lower angles,[25,61,67,68] while LLZO prepared using conventional pressureless sintering displays a higher percentage of grain boundaries with lower misorientation angles.[12] On the basis that the P2G method is not only a pressureless method but also one that utilizes liquid phase sintering as well as reactive sintering, it is plausible that the grain boundary misorientation angles (and other properties, *e.g.*, mechanical) could be different in P2G compared to those seen in hot-pressed and conventionally sintered LLZO.

Second, the deleterious effects of compositional inhomogeneity may be mitigated *via* the P2G process. Our previous studies on LLZTO showed that inhomogeneous distribution of the Ta-dopant among various grains can lead to lower ionic conductivity and that the P2G method is one approach to mitigate composition inhomogeneity.[69] Not only is compositional uniformity important for achieving high ionic conductivity and stabilization of the cubic phase of LLZTO, but since Zr has been demonstrated to be less stable to reduction by Li metal compared to Ta,[64,70] grains with local Zr enrichment could be susceptible to the formation of electronically conducting pathways.

5. CONCLUSIONS

In summary, we show that P2G LLZTO pellets prepared *via* reactive sintering of Ta-doped pyrochlores with LiOH can display a higher CCD and voltage compared to LLZTO prepared using SSR and conventional pressureless sintering. Despite the smaller grain sizes and higher grain boundary area in P2G LLZTO, we observe improved resistance to Li dendrite nucleation and propagation around the grain boundaries, in stark contrast to the failure mechanism seen in SSR LLZTO. We believe that this is due to the more distributed Li^+ ion current density through P2G LLZO pellets containing a larger number of grain boundaries (*i.e.*, from smaller grain sizes) compared to the more focused current at fewer failure points in SSR LLZO with larger grain sizes. This study highlights how different synthesis and sintering methods may lead to different cycling outcomes and failure modes. Further comprehensive studies on how grain boundary properties vary in LLZO prepared using different methods may be worthwhile for obtaining a more fundamental understanding of the failure mechanisms and opportunities for improving garnet-type solid electrolytes for use in solid-state Li metal batteries.

■ ASSOCIATED CONTENT

Supporting Information

The Supporting Information is available free of charge at https://pubs.acs.org/doi/10.1021/acsami.3c11421.

Detailed properties of LLZTO pellets; relationship between ionic conductivity and relative density for SSR and P2G LLZTO pellets prepared with different sintering conditions; Nyquist plots of P2G and SSR pellets taken from −20 to 60 °C; XRD patterns of P2G and SSR pellets; XPS data of P2G pellet before and after Ar^+ etching; Zr 3d XPS data for the mixture of SSR LLZTO, Ta_2O_5, and ZrO_2; comparison of La 3d and Zr 3d XPS spectra from SSR and P2G LLZTO; chronoamperometry curves for SSR and P2G pellets used to obtain electronic conductivity; Nyquist plots of P2G and SSR pellets prior to galvanostatic Li stripping/plating; zoom-in voltage profiles from Li stripping/plating measurements; additional Li stripping/plating curves to show reproducibility; Nyquist plots of P2G and SSR pellets prior to LSV; additional SEM images of SSR and P2G pellets after Li stripping/plating; EDS map and spectrum of SSR pellet with Mg and Al contamination; EDS spectra of pyrochlore and P2G pellet; Li stripping/plating, EDS, and impedance data from contamination-free SSR pellet; and micrograph comparison of P2G grains with garnet mineralogical specimens (PDF)

https://doi.org/10.1021/acsami.3c11421
ACS Appl. Mater. Interfaces 2024, 16, 4519−4529

AUTHOR INFORMATION

Corresponding Author

Candace K. Chan − *Materials Science and Engineering, School for Engineering of Matter, Transport and Energy, Arizona State University, Tempe, Arizona 85827, United States;* orcid.org/0000-0003-4329-4865; Phone: (480) 727-8614; Email: candace.chan@asu.edu

Author

Jinzhao Guo − *Materials Science and Engineering, School for Engineering of Matter, Transport and Energy, Arizona State University, Tempe, Arizona 85827, United States;* orcid.org/0000-0001-7397-0786

Complete contact information is available at: https://pubs.acs.org/10.1021/acsami.3c11421

Author Contributions

The manuscript was written through contributions of both authors. J.G. performed the synthesis, electrochemical measurements, materials characterization, and data analysis. C.K.C. assisted with the data interpretation. Both authors have given approval to the final version of the manuscript.

Notes

The authors declare no competing financial interest.

ACKNOWLEDGMENTS

This work was supported by funding from the National Science Foundation (NSF) from the awards DMR-1553519 and CMMI-1929806. The authors acknowledge the use of facilities within the Eyring Materials Center (supported in part by NNCI-ECCS-1542160). The authors thank X. Guo for assistance with XPS and REELs measurements, D. Nguyen for assistance with SSR LLZTO synthesis, M.H. Bhat for assistance with the low-temperature impedance measurements, and J.M. Weller for helpful discussions.

REFERENCES

(1) Murugan, R.; Thangadurai, V.; Weppner, W. Fast Lithium Ion Conduction in Garnet-type $Li_7La_3Zr_2O_{12}$. *Angew. Chem., Int. Ed.* **2007**, *46* (41), 7778−7781.

(2) Wang, Y.; Lai, W. High Ionic Conductivity Lithium Garnet Oxides of $Li_{7-x}La_3Zr_{2-x}Ta_xO_{12}$ Compositions. *Electrochem. Solid State Lett.* **2012**, *15* (5), A68.

(3) Rangasamy, E.; Wolfenstine, J.; Sakamoto, J. The Role of Al and Li Concentration on the Formation of Cubic Garnet Solid Electrolyte of Nominal Composition $Li_7La_3Zr_2O_{12}$. *Solid State Ionics* **2012**, *206*, 28−32.

(4) Huang, X.; Lu, Y.; Song, Z.; Rui, K.; Wang, Q.; Xiu, T.; Badding, M. E.; Wen, Z. Manipulating Li_2O Atmosphere for Sintering Dense $Li_7La_3Zr_2O_{12}$ Solid Electrolyte. *Energy Storage Mater.* **2019**, *22*, 207−217.

(5) Weller, J. M.; Chan, C. K. Pyrochlore Nanocrystals as Versatile Quasi-Single-Source Precursors to Lithium Conducting Garnets. *J. Mater. Chem. A* **2020**, *8* (34), 17405−17410.

(6) Guo, J.; Weller, J. M.; Yang, S.; Bhat, M. H.; Chan, C. K. Reactive Sintering of Garnet-Type $Li_{6.4}La_3Zr_{1.4}Ta_{0.6}O_{12}$ (LLZTO) from Pyrochlore Precursors Prepared Using a Non-Aqueous Sol-Gel Method. *Ionics* **2023**, *29*, 581−590.

(7) Kiat, J.; Boemare, G.; Rieu, B.; Aymes, D. Structural Evolution of LiOH: Evidence of a Solid-Solid Transformation toward Li_2O Close to the Melting Temperature. *Solid State Commun.* **1998**, *108* (4), 241−245.

(8) Chiang, Y. M.; Lavik, E. B.; Kosacki, I.; Tuller, H. L.; Ying, J. Y. Defect and Transport Properties of Nanocrystalline CeO_{2-x}. *Appl. Phys. Lett.* **1996**, *69* (2), 185−187.

(9) Wen, Z.; Xu, X.; Li, J. Preparation, Microstructure and Electrical Properties of $Li_{1.4}Al_{0.4}Ti_{1.6}(PO_4)_3$ Nanoceramics. *J. Electroceram.* **2009**, *22* (1−3), 342−345.

(10) Tenhaeff, W. E.; Rangasamy, E.; Wang, Y.; Sokolov, A. P.; Wolfenstine, J.; Sakamoto, J.; Dudney, N. J. Resolving the Grain Boundary and Lattice Impedance of Hot-Pressed $Li_7La_3Zr_2O_{12}$ Garnet Electrolytes. *ChemElectroChem.* **2014**, *1* (2), 375−378.

(11) Cheng, L.; Park, J. S.; Hou, H.; Zorba, V.; Chen, G.; Richardson, T.; Cabana, J.; Russo, R.; Doeff, M. Effect of Microstructure and Surface Impurity Segregation on the Electrical and Electrochemical Properties of Dense Al-Substituted $Li_7La_3Zr_2O_{12}$. *J. Mater. Chem. A* **2014**, *2* (1), 172−181.

(12) Cheng, L.; Chen, W.; Kunz, M.; Persson, K.; Tamura, N.; Chen, G.; Doeff, M. Effect of Surface Microstructure on Electrochemical Performance of Garnet Solid Electrolytes. *ACS Appl. Mater. Interfaces* **2015**, *7* (3), 2073−2081.

(13) Cheng, L.; Wu, C. H.; Jarry, A.; Chen, W.; Ye, Y.; Zhu, J.; Kostecki, R.; Persson, K.; Guo, J.; Salmeron, M.; et al. Interrelationships among Grain Size, Surface Composition, Air Stability, and Interfacial Resistance of Al-Substituted $Li_7La_3Zr_2O_{12}$ Solid Electrolytes. *ACS Appl. Mater. Interfaces* **2015**, *7* (32), 17649−17655.

(14) Sakamoto, J.; Rangasamy, E.; Kim, H.; Kim, Y.; Wolfenstine, J. Synthesis of Nano-scale Fast Ion Conducting Cubic $Li_7La_3Zr_2O_{12}$. *Nanotechnology* **2013**, *24* (42), 424005.

(15) Matsuki, Y.; Noi, K.; Deguchi, M.; Sakuda, A.; Hayashi, A.; Tatsumisago, M. Lithium Dissolution/Deposition Behavior of Al-doped $Li_7La_3Zr_2O_{12}$ Ceramics with Different Grain Sizes. *J. Electrochem. Soc.* **2019**, *166* (3), A5470−A5473.

(16) Ren, Y.; Shen, Y.; Lin, Y.; Nan, C.-W. Microstructure Manipulation for Enhancing the Resistance of Garnet-Type Solid Electrolytes to "Short Circuit" by Li Metal Anodes. *ACS Appl. Mater. Interfaces* **2019**, *11* (6), 5928−5937.

(17) Sharafi, A.; Haslam, C. G.; Kerns, R. D.; Wolfenstine, J.; Sakamoto, J. Controlling and Correlating the Effect of Grain Size With the Mechanical and Electrochemical Properties of $Li_7La_3Zr_2O_{12}$ Solid-State Electrolyte. *J. Mater. Chem. A* **2017**, *5* (40), 21491−21504.

(18) Ren, Y.; Shen, Y.; Lin, Y.; Nan, C.-W. Direct Observation of Lithium Dendrites Inside Garnet-Type Lithium-Ion Solid Electrolyte. *Electrochem. Commun.* **2015**, *57*, 27−30.

(19) Suzuki, Y.; Kami, K.; Watanabe, K.; Watanabe, A.; Saito, N.; Ohnishi, T.; Takada, K.; Sudo, R.; Imanishi, N. Transparent Cubic Garnet-Type Solid Electrolyte of Al_2O_3-Doped $Li_7La_3Zr_2O_{12}$. *Solid State Ionics* **2015**, *278*, 172−176.

(20) Cheng, E. J.; Sharafi, A.; Sakamoto, J. Intergranular Li Metal Propagation Through Polycrystalline $Li_{6.25}Al_{0.25}La_3Zr_2O_{12}$ Ceramic Electrolyte. *Electrochim. Acta* **2017**, *223*, 85−91.

(21) Han, F.; Westover, A. S.; Yue, J.; Fan, X.; Wang, F.; Chi, M.; Leonard, D. N.; Dudney, N. J.; Wang, H.; Wang, C. High Electronic Conductivity as the Origin of Lithium Dendrite Formation Within Solid Electrolytes. *Nat. Energy* **2019**, *4* (3), 187−196.

(22) Song, Y.; Yang, L.; Tao, L.; Zhao, Q.; Wang, Z.; Cui, Y.; Liu, H.; Lin, Y.; Pan, F. Probing into the Origin of an Electronic Conductivity Surge in a Garnet Solid-State Electrolyte. *J. Mater. Chem. A* **2019**, *7* (40), 22898−22902.

(23) Tian, H.-K.; Liu, Z.; Ji, Y.; Chen, L.-Q.; Qi, Y. Interfacial Electronic Properties Dictate Li Dendrite Growth in Solid Electrolytes. *Chem. Mater.* **2019**, *31* (18), 7351−7359.

(24) Song, Y.; Yang, L.; Zhao, W.; Wang, Z.; Zhao, Y.; Wang, Z.; Zhao, Q.; Liu, H.; Pan, F. Revealing the Short-Circuiting Mechanism of Garnet-Based Solid-State Electrolyte. *Adv. Energy Mater.* **2019**, *9* (21), 1900671.

(25) Liu, X.; Garcia-Mendez, R.; Lupini, A. R.; Cheng, Y.; Hood, Z. D.; Han, F.; Sharafi, A.; Idrobo, J. C.; Dudney, N. J.; Wang, C.; et al. Local Electronic Structure Variation Resulting in Li 'Filament' Formation Within Solid Electrolytes. *Nat. Mater.* **2021**, *20*, 1485−1490.

(26) Kim, J.-S.; Kim, H.; Badding, M.; Song, Z.; Kim, K.; Kim, Y.; Yun, D.-J.; Lee, D.; Chang, J.; Kim, S.; et al. Origin of Intergranular Li Metal Propagation in Garnet-based Solid Electrolyte by Direct

Electronic Structure Analysis and Performance Improvement by Bandgap Engineering. *J. Mater. Chem. A* **2020**, *8* (33), 16892−16901.
(27) Tian, H.-K.; Xu, B.; Qi, Y. Computational Study of Lithium Nucleation Tendency in $Li_7La_3Zr_2O_{12}$ (LLZO) and Rational Design of Interlayer Materials to Prevent Lithium Dendrites. *J. Power Sources* **2018**, *392*, 79−86.
(28) Zhu, C.; Fuchs, T.; Weber, S. A. L.; Richter, F. H.; Glasser, G.; Weber, F.; Butt, H.-J.; Janek, J.; Berger, R. Understanding the Evolution of Lithium Dendrites at $Li_{6.25}Al_{0.25}La_3Zr_2O_{12}$ Grain Boundaries via Operando Microscopy Techniques. *Nat. Commun.* **2023**, *14* (1), 1300.
(29) Yu, S.; Siegel, D. J. Grain Boundary Softening: a Potential Mechanism for Lithium Metal Penetration Through Stiff Solid Electrolytes. *ACS Appl. Mater. Interfaces* **2018**, *10* (44), 38151−38158.
(30) Tantratian, K.; Yan, H.; Ellwood, K.; Harrison, E. T.; Chen, L. Unraveling the Li Penetration Mechanism in Polycrystalline Solid Electrolytes. *Adv. Energy Mater.* **2021**, *11* (13), 2003417.
(31) Shiiba, H.; Zettsu, N.; Yamashita, M.; Onodera, H.; Jalem, R.; Nakayama, M.; Teshima, K. Molecular Dynamics Studies on the Lithium Ion Conduction Behaviors Depending on Tilted Grain Boundaries with Various Symmetries in Garnet-Type $Li_7La_3Zr_2O_{12}$. *J. Phys. Chem. C* **2018**, *122* (38), 21755−21762.
(32) Weller, J. M.; Whetten, J. A.; Chan, C. K. Nonaqueous Polymer Combustion Synthesis of Cubic $Li_7La_3Zr_2O_{12}$ Nanopowders. *ACS Appl. Mater. Interfaces* **2020**, *12* (1), 953−962.
(33) Li, Y.; Han, J.-T.; Wang, C.-A.; Xie, H.; Goodenough, J. B. Optimizing Li^+ Conductivity in a Garnet Framework. *J. Mater. Chem.* **2012**, *22* (30), 15357−15361.
(34) Kim, K. S.; Baitinger, W. E.; Winograd, N. X-ray Photoelectron Spectroscopic Studies of PbO Surfaces Bombarded with He^+, Ne^+, Ar^+, Xe^+ and Kr^+. *Surf. Sci.* **1976**, *55* (1), 285−290.
(35) Kim, J.-N.; Shin, K.-S.; Kim, D.-H.; Park, B.-O.; Kim, N.-K.; Cho, S.-H. Changes in Chemical Behavior of Thin Film Lead Zirconate Titanate During Ar^+ Ion Bombardment Using XPS. *Appl. Surf. Sci.* **2003**, *206* (1−4), 119−128.
(36) Bespalov, I.; Datler, M.; Buhr, S.; Drachsel, W.; Rupprechter, G.; Suchorski, Y. Initial Stages of Oxide Formation on the Zr Surface at Low Oxygen Pressure: An In Situ FIM and XPS Study. *Ultramicroscopy* **2015**, *159*, 147−151.
(37) Azdad, Z.; Marot, L.; Moser, L.; Steiner, R.; Meyer, E. Valence Band Behaviour of Zirconium Oxide, Photoelectron and Auger Spectroscopy Study. *Sci. Rep.* **2018**, *8* (1), 16251.
(38) Vos, M.; King, S. W.; French, B. L. Measurement of the Band Gap by Reflection Electron Energy Loss Spectroscopy. *J. Electron Spectrosc. Relat. Phenom.* **2016**, *212*, 74−80.
(39) Heo, S.; Cho, E.; Lee, H.-I.; Park, G. S.; Kang, H. J.; Nagatomi, T.; Choi, P.; Choi, B.-D. Band Gap and Defect States of MgO Thin Films Investigated Using Reflection Electron Energy Loss Spectroscopy. *AIP Adv.* **2015**, *5* (7), 077167.
(40) Wang, C.; Xie, H.; Zhang, L.; Gong, Y.; Pastel, G.; Dai, J.; Liu, B.; Wachsman, E. D.; Hu, L. Universal Soldering of Lithium and Sodium Alloys on Various Substrates for Batteries. *Adv. Energy Mater.* **2018**, *8* (6), 1701963.
(41) Weller, J. M.; Chan, C. K. Reduction in Formation Temperature of Ta-Doped Lithium Lanthanum Zirconate by Application of Lux-Flood Basic Molten Salt Synthesis. *ACS Appl. Energy Mater.* **2020**, *3* (7), 6466−6475.
(42) Xia, W.; Xu, B.; Duan, H.; Tang, X.; Guo, Y.; Kang, H.; Li, H.; Liu, H. Reaction Mechanisms of Lithium Garnet Pellets in Ambient Air: The Effect of Humidity and CO_2. *J. Am. Ceram. Soc.* **2017**, *100* (7), 2832−2839.
(43) Ikawa, H.; Yamada, T.; Kojima, K.; Matsumoto, S. X-ray Photoelectron Spectroscopy Study of High- and Low-Temperature Forms of Zirconium Titanate. *J. Am. Ceram. Soc.* **1991**, *74* (6), 1459−1462.
(44) Gao, Y.; Sun, S.; Zhang, X.; Liu, Y.; Hu, J.; Huang, Z.; Gao, M.; Pan, H. Amorphous Dual-Layer Coating: Enabling High Li-Ion Conductivity of Non-Sintered Garnet-Type Solid Electrolyte. *Adv. Funct. Mater.* **2021**, *31* (15), 2009692.
(45) Lecuyer, S.; Quemerais, A.; Jezequel, G. Composition of Natural Oxide Films on Polycrystalline Tantalum using XPS Electron Take-off Angle Experiments. *Surf. Interface Anal.* **1992**, *18* (4), 257−261.
(46) Kerrec, O.; Devilliers, D.; Groult, H.; Marcus, P. Study of Dry and Electrogenerated Ta_2O_5 and $Ta/Ta_2O_5/Pt$ Structures by XPS. *Mater. Sci. Eng. B* **1998**, *55* (1−2), 134−142.
(47) Hashimoto, S.; Tanaka, C.; Murata, A.; Sakurada, T. Formulation for XPS Spectral Change of Oxides by Ar Ion Bombardment: Application of the Formulation to Ta. *J. Surf. Anal.* **2006**, *13* (1), 14−18.
(48) Alov, N. V. Surface Oxidation of Metals by Oxygen Ion Bombardment. *Nucl. Instrum. Methods Phys. Res., Sect. B* **2007**, *256* (1), 337−340.
(49) Khanuja, M.; Sharma, H.; Mehta, B. R.; Shivaprasad, S. M. XPS Depth-Profile of the Suboxide Distribution at the Native Oxide/Ta Interface. *J. Electron Spectrosc. Relat. Phenom.* **2009**, *169* (1), 41−45.
(50) Erskine, J. Electron Energy Loss Spectroscopy in Analysis of Surfaces. *Encyclopedia of Analytical Chemistry: Applications, Theory and Instrumentation*; Wiley, 2000.
(51) Ajith, K.; Christopher Selvin, P.; Abhilash, K. P.; Sivaraj, P.; Nalini, B.; Soundarya, G. G. A Correlative Study on Electrochemical and Optical Properties of LLZO ($Li_7La_3Zr_2O_{12}$) Garnet Electrolyte. *Mater. Today: Proc.* **2022**, *50*, 2836−2839.
(52) Thompson, T.; Yu, S.; Williams, L.; Schmidt, R. D.; Garcia-Mendez, R.; Wolfenstine, J.; Allen, J. L.; Kioupakis, E.; Siegel, D. J.; Sakamoto, J. Electrochemical Window of the Li-Ion Solid Electrolyte $Li_7La_3Zr_2O_{12}$. *ACS Energy Lett.* **2017**, *2* (2), 462−468.
(53) Huang, M.; Liu, T.; Deng, Y.; Geng, H.; Shen, Y.; Lin, Y.; Nan, C.-W. Effect of Sintering Temperature on Structure and Ionic Conductivity of $Li_{7-x}La_3Zr_2O_{12-0.5x}$ (x = 0.5 ∼ 0.7) Ceramics. *Solid State Ionics* **2011**, *204−205*, 41−45.
(54) Sastre, J.; Priebe, A.; Döbeli, M.; Michler, J.; Tiwari, A. N.; Romanyuk, Y. E. Lithium Garnet $Li_7La_3Zr_2O_{12}$ Electrolyte for All-Solid-State Batteries: Closing the Gap between Bulk and Thin Film Li-Ion Conductivities. *Adv. Mater. Interfaces* **2020**, *7* (17), 2000425.
(55) Gopal, R.; Wu, L.; Lee, Y.; Guo, J.; Bai, P. Transient Polarization and Dendrite Initiation Dynamics in Ceramic Electrolytes. *ACS Energy Lett.* **2023**, *8* (5), 2141−2149.
(56) Ouyang, C.; Zheng, H.; Chen, Q.; Liu, H.; Duan, H. Correlating the Microstructure and Current Density of the Li/Garnet Interface. *ACS Appl. Mater. Interfaces* **2023**, *15* (44), 51179−51190.
(57) Geiger, C. A.; Alekseev, E.; Lazic, B.; Fisch, M.; Armbruster, T.; Langner, R.; Fechtelkord, M.; Kim, N.; Pettke, T.; Weppner, W. Crystal Chemistry and Stability of "$Li_7La_3Zr_2O_{12}$" Garnet: A Fast Lithium-Ion Conductor. *Inorg. Chem.* **2011**, *50* (3), 1089−1097.
(58) El-Shinawi, H.; Paterson, G. W.; MacLaren, D. A.; Cussen, E. J.; Corr, S. A. Low-Temperature Densification of Al-Doped $Li_7La_3Zr_2O_{12}$: a Reliable and Controllable Synthesis of Fast-Ion Conducting Garnets. *J. Mater. Chem. A* **2017**, *5* (1), 319−329.
(59) Philipp, M.; Gadermaier, B.; Posch, P.; Hanzu, I.; Ganschow, S.; Meven, M.; Rettenwander, D.; Redhammer, G. J.; Wilkening, H. M. R. The Electronic Conductivity of Single Crystalline Ga-Stabilized Cubic $Li_7La_3Zr_2O_{12}$: A Technologically Relevant Parameter for All-Solid-State Batteries. *Adv. Mater. Interfaces* **2020**, *7* (16), 2000450.
(60) Squires, A. G.; Davies, D. W.; Kim, S.; Scanlon, D. O.; Walsh, A.; Morgan, B. J. Low Electronic Conductivity of $Li_7La_3Zr_2O_{12}$ Solid Electrolytes from First Principles. *Phys. Rev. Mater.* **2022**, *6* (8), 085401.
(61) Sharafi, A.; Kazyak, E.; Davis, A. L.; Yu, S.; Thompson, T.; Siegel, D. J.; Dasgupta, N. P.; Sakamoto, J. Surface Chemistry Mechanism of Ultra-Low Interfacial Resistance in the Solid-State Electrolyte $Li_7La_3Zr_2O_{12}$. *Chem. Mater.* **2017**, *29* (18), 7961−7968.
(62) Wang, D.; Zhu, C.; Fu, Y.; Sun, X.; Yang, Y. Interfaces in Garnet-Based All-Solid-State Lithium Batteries. *Adv. Energy Mater.* **2020**, *10* (39), 2001318.

https://doi.org/10.1021/acsami.3c11421
ACS Appl. Mater. Interfaces 2024, 16, 4519−4529

(63) Su, J.; Huang, X.; Song, Z.; Xiu, T.; Badding, M. E.; Jin, J.; Wen, Z. Overcoming the Abnormal Grain Growth in Ga-Doped $Li_7La_3Zr_2O_{12}$ to Enhance the Electrochemical Stability Against Li Metal. *Ceram. Int.* **2019**, *45* (12), 14991−14996.
(64) Gao, B.; Jalem, R.; Tateyama, Y. Surface-Dependent Stability of the Interface between Garnet $Li_7La_3Zr_2O_{12}$ and the Li Metal in the All-Solid-State Battery from First-Principles Calculations. *ACS Appl. Mater. Interfaces* **2020**, *12* (14), 16350−16358.
(65) German, R. M.; Suri, P.; Park, S. J. Review: Liquid Phase Sintering. *J. Mater. Sci.* **2009**, *44* (1), 1−39.
(66) Seaman, D. M.; Gallant, R. P. Spessartite Garnet with Hexoctahedral Faces from Jail Hill, Haddam, Connecticut. *Rocks Miner.* **1960**, *35* (9−10), 445−448.
(67) Moy, A. C.; Häuschen, G.; Fattakhova-Rohlfing, D.; Wolfenstine, J. B.; Finsterbusch, M.; Sakamoto, J. The Effects of Aluminum Concentration on the Microstructural and Electrochemical Properties of Lithium Lanthanum Zirconium Oxide. *J. Mater. Chem. A* **2022**, *10* (41), 21955−21972.
(68) Fu, S.; Arinicheva, Y.; Hüter, C.; Finsterbusch, M.; Spatschek, R. Grain Boundary Characterization and Potential Percolation of the Solid Electrolyte LLZO. *Batteries* **2023**, *9* (4), 222.
(69) Weller, J. M.; Dopilka, A.; Chan, C. K. Observation of Elemental Inhomogeneity and Its Impact on Ionic Conductivity in Li-Conducting Garnets Prepared with Different Synthesis Methods. *Adv. Energy Sustainability Res.* **2021**, *2* (5), 2000109.
(70) Zhu, Y.; Connell, J. G.; Tepavcevic, S.; Zapol, P.; Garcia-Mendez, R.; Taylor, N. J.; Sakamoto, J.; Ingram, B. J.; Curtiss, L. A.; Freeland, J. W.; et al. Dopant-Dependent Stability of Garnet Solid Electrolyte Interfaces with Lithium Metal. *Adv. Energy Mater.* **2019**, *9* (12), 1803440.

https://doi.org/10.1021/acsami.3c11421
ACS Appl. Mater. Interfaces 2024, 16, 4519−4529